Rippled area formed by surface plasmon polaritons upon femtosecond laser double-pulse irradiation of silicon

Thibault J. Y. Derrien, Jörg Krüger, Tatiana Itina, Sandra Höhm, Arkadi Rosenfeld, Jörn Bonse

Rippled area formed by surface plasmon polaritons upon femtosecond laser double-pulse irradiation of silicon

Thibault J.-Y. Derrien,[1,*] Jörg Krüger,[1] Tatiana E. Itina,[2] Sandra Höhm,[3] Arkadi Rosenfeld,[3] and Jörn Bonse[1]

[1] *BAM Bundesanstalt für Materialforschung und -prüfung, Unter den Eichen 87, D-12205 Berlin, Germany*

[2] *Laboratoire Hubert Curien (LabHC), UMR CNRS 5516 - Université Jean Monnet, Bat. F, 18 rue du Professeur Benoit Lauras, 42000 Saint-Etienne, France*

[3] *Max-Born-Institut für Nichtlineare Optik und Kurzzeitspektroskopie (MBI), Max-Born-Straße 2A, D-12489 Berlin, Germany*

[*] *thibault.derrien@bam.de*

Abstract: The formation of near-wavelength laser-induced periodic surface structures (LIPSS) on silicon upon irradiation with sequences of Ti:sapphire femtosecond laser pulse pairs (pulse duration 150 fs, central wavelength 800 nm) is studied theoretically. For this purpose, the nonlinear generation of conduction band electrons in silicon and their relaxation is numerically calculated using a two-temperature model approach including intrapulse changes of optical properties, transport, diffusion and recombination effects. Following the idea that surface plasmon polaritons (SPP) can be excited when the material turns from semiconducting to metallic state, the "SPP active area" is calculated as function of fluence and double-pulse delay up to several picoseconds and compared to the experimentally observed rippled surface areas. Evidence is presented that multi-photon absorption explains the large increase of the rippled area for temporally overlapping pulses. For longer double-pulse delays, relevant relaxation processes are identified. The results demonstrate that femtosecond LIPSS on silicon are caused by the excitation of SPP and can be controlled by temporal pulse shaping.

OCIS codes: (050.6624) Subwavelength structures; (140.3390) Laser materials processing; (160.6000) Semiconductor materials; (240.5420) Polaritons.

References

1. A. Borowiec and H. K. Haugen, "Subwavelength ripple formation on the surfaces of compound semiconductors irradiated with femtosecond laser pulses," Appl. Phys. Lett. **82**, 4462–4464 (2003).
2. R. Wagner and J. Gottmann, "Sub-wavelength ripple formation on various materials induced by tightly focused femtosecond laser radiation," J. Phys. Conf. Ser. **59**, 333–337 (2007).
3. M. Huang, F. Zhao, Y. Cheng, N. Xu, and Z. Xu, "Origin of laser-induced near-subwavelength ripples: Interference between surface plasmons and incident laser," ACS Nano **3**, 4062–4070 (2009).
4. U. Chakravarty, R. Ganeev, P. Naik, J. Chakera, M. Babu, and P. Gupta, "Nano-ripple formation on different band-gap semiconductor surfaces using femtosecond pulses," J. Appl. Phys. **109**, 084347 (2011).
5. J. Bonse, J. Krüger, S. Höhm, and A. Rosenfeld, "Femtosecond laser-induced periodic surface structures," J. Laser Appl. **24**, 042006 (2012).
6. J. E. Sipe, J. F. Young, J. Preston, and H. V. Driel, "Laser-induced periodic surface structure. I. Theory," Phys. Rev. B **27**, 1141–1154 (1983).

#197904 - $15.00 USD Received 17 Sep 2013; revised 23 Oct 2013; accepted 27 Oct 2013; published 22 Nov 2013

7. A. M. Bonch-Bruevich, M. N. Libenson, V. S. Makin, and V. A. Trubaev, "Surface electromagnetic waves in optics," Opt. Eng. **31**, 718–730 (1992).
8. J. Reif, F. Costache, M. Henyk, and S. V. Pandelov, "Ripples revisited - non-classical morphology at the bottom of femtosecond laser ablation craters in transparent dielectrics," Appl. Surf. Sci. **197–198**, 891–895 (2002).
9. D. Dufft, A. Rosenfeld, S. K. Das, R. Grunwald, and J. Bonse, "Femtosecond laser-induced periodic surface structures revisited - a comparative study on ZnO," J. Appl. Phys. **105**, 034908 (2009).
10. J. Bonse, S. Baudach, J. Krüger, W. Kautek, and M. Lenzner, "Femtosecond laser ablation of silicon-modification thresholds and morphology," Appl. Phys. A **74**, 19–25 (2002).
11. F. Costache, S. Kouteva-Arguirova, and J. Reif, "Sub-damage-threshold femtosecond laser ablation from crystalline Si: surface nanostructures and phase transformation," Appl. Phys. A **79**, 1429–1432 (2004).
12. M. Guillermin, F. Garrelie, N. Sanner, E. Audouard, and H. Soder, "Single and multi-pulse formation of surface structures under static femtosecond irradiation," Appl. Surf. Sci. **253**, 8075–8079 (2007).
13. J. Bonse, A. Rosenfeld, and J. Krüger, "On the role of surface plasmon polaritons in the formation of laser-induced periodic surface structures upon irradiation of silicon by femtosecond-laser pulses," J. Appl. Phys. **106**, 104910 (2009).
14. J. Bonse and J. Krüger, "Pulse number dependence of laser-induced periodic surface structures for femtosecond laser irradiation of silicon," J. Appl. Phys. **108**, 034903 (2010).
15. T. J.-Y. Derrien, T. E. Itina, R. Torres, T. Sarnet, and M. Sentis, "Possible surface plasmon polariton excitation under femtosecond laser irradiation of silicon," J. Appl. Phys. **114**, 083104 (2013).
16. G. A. Martsinovskii, G. D. Shandybina, D. S. Smirnov, S. V. Zabotnov, L. A. Golovan, V. Y. Timoshenko, and P. K. Kashkarov, "Ultrashort excitations of surface polaritons and waveguide modes in semiconductors," Opt. Spectrosc. **105**, 67–72 (2008).
17. T. J.-Y. Derrien, T. Sarnet, M. Sentis, and T. E. Itina, "Application of a two-temperature model for the investigation of the periodic structure formation on Si surface in femtosecond laser interactions," J. Optoelectron. Adv. Mater. **12**, 610–615 (2010).
18. G. Tsibidis, M. Barberoglou, P. Loukakos, E. Stratakis, and C. Fotakis, "Dynamics of ripple formation on silicon surfaces by ultrashort laser pulses in subablation conditions," Phys. Rev. B **86**, 115316 (2012).
19. T. J.-Y. Derrien, "Nanostructuration de cellules photovoltaiques par impulsion laser femtoseconde. etude des mécanismes de formation," Ph.D. thesis, Université de la Méditerranée - Aix Marseille II (2012).
20. T. Crawford, G. Botton, and H. Haugen, "Crystalline orientation effects on conical structure formation in femtosecond laser irradiation of silicon and germanium," Appl. Surf. Sci. **256**, 1749–1755 (2010).
21. K. Sokolowski-Tinten, A. Barty, S. Boutet, U. Shymanovich, H. Chapman, M. Bogan, S. Marchesini, S. Hau-Riege, N. Stojanovic, J. Bonse, Y. Rosandi, H. M. Urbassek, R. Tobey, H. Ehrke, A. Cavalleri, S. Düsterer, H. Redlin, M. Frank, S. Bajt, J. Schulz, M. Seibert, J. Hajdu, R. Treusch, C. Bostedt, M. Hoener, and T. Möller, "Short-pulse laser induced transient structure formation and ablation studied with time-resolved coherent xuv-scattering," AIP Conf. Proc. **1278**, 373–379 (2010).
22. S. Höhm, A. Rosenfeld, J. Krüger, and J. Bonse, "Area dependence of femtosecond laser-induced periodic surface structures for varying band gap materials after double pulse excitation," Appl. Surf. Sci. **278**, 7–12 (2013).
23. S. Höhm, M. Rohloff, A. Rosenfeld, J. Krüger, and J. Bonse, "Dynamics of the formation of laser-induced periodic surface structures on dielectrics and semiconductors upon femtosecond laser pulse irradiation sequences," Appl. Phys. A **110**, 553–557 (2013).
24. J. E. Sipe and H. V. Driel, "Laser induced periodic surface structure: an experimental and theoretical review," Proc. SPIE **1033**, 302–318 (1988).
25. N. M. Bulgakova, R. Stoian, A. Rosenfeld, I. V. Hertel, W. Marine, and E. E. B. Campbell, "A general continuum approach to describe fast electronic transport in pulsed laser irradiated materials - the problem of coulomb explosion," Appl. Phys. A **81**, 345–356 (2005).
26. C. Shank, R. Yen, and C. Hirlimann, "Time-resolved reflectivity measurements of femtosecond-optical-pulse-induced phase transitions in silicon," Phys. Rev. Lett. **50**, 454–457 (1983).
27. K. Sokolowski-Tinten and D. von der Linde, "Generation of dense electron-hole plasmas in silicon," Phys. Rev. B **61**, 2643–2650 (2000).
28. H. Raether, *Surface Plasmons on Smooth and Rough Surfaces and on Gratings* (Springer, 1986).
29. E. D. Palik, *Handbook of Optical Constants of Solids* (Academic, 1985).
30. D. Bäuerle, *Laser Processing and Chemistry* (Springer, 2011), 4th ed.
31. N. M. Bulgakova, R. Stoian, and A. Rosenfeld, "Laser-induced modification of transparent crystals and glasses," Quantum Electron. **40**, 966–985 (2010).
32. J. D. Jackson, *Classical Electrodynamics*, 3rd ed. (Wiley, 1999).
33. T. Sjodin, H. Petek, and H.-L. Dai, "Ultrafast carrier dynamics in silicon: A two-color transient reflection grating study on a (111) surface," Phys. Rev. Lett. **81**, 5664–5667 (1998).
34. E. J. Yoffa, "Dynamics of dense laser-induced plasmas," Phys. Rev. B **21**, 2415–2425 (1980).
35. H. V. Driel, "Kinetics of high-density plasmas generated in Si by 1.06- and 0.53-μm picosecond laser pulses," Phys. Rev. B **35**, 8166–8176 (1987).
36. A. Sabbah and D. Riffe, "Femtosecond pump-probe reflectivity study of silicon carrier dynamics," Phys. Rev. B

#197904 - $15.00 USD Received 17 Sep 2013; revised 23 Oct 2013; accepted 27 Oct 2013; published 22 Nov 2013

66, 165217 (2002).
37. M. Harb, R. Ernstorfer, T. Dartigalongue, C. T. Hebeisen, R. E. Jordan, and R. J. D. Miller, "Carrier relaxation and lattice heating dynamics in silicon revealed by femtosecond electron diffraction," J. Phys. Chem. B **110**, 25308–25313 (2006).
38. P. Desai, "Thermodynamic properties of iron and silicon," J. Phys. Chem. Ref. Data **15**, 967–983 (1986).
39. A. L. Magna, P. Alippi, V. Privitera, G. Fortunato, M. Camalleri, and B. Svensson, "A phase-field approach to the simulation of the excimer laser annealing process in Si," J. Appl. Phys. **95**, 4806–4814 (2004).
40. W.-K. Rhim and K. Ohsaka, "Thermophysical properties measurement of molten silicon by high-temperature electrostatic levitator: density, volume expansion, specific heat capacity, emissivity, surface tension and viscosity," J. Cryst. Growth **208**, 313–321 (2000).
41. D. Korfiatis, K. Thoma, and J. Vardaxoglou, "Conditions for femtosecond laser melting of silicon," J. Phys. D Appl. Phys. **40**, 6803–6808 (2007).
42. H. Versteeg and W. Malalasekera, *An Introduction to Computational Fluid Dynamics - The Finite Volume Method* (Pearson Education, 2007).
43. W. H. Press, S. A. Teukolsky, W. T. Vetterling, and B. P. Flannery, *Numerical Recipes: The Art of Scientific Computing* (Cambridge University, 2007).
44. J. Bonse, M. Munz, and H. Sturm, "Structure formation on the surface of indium phosphide irradiated by femtosecond laser pulses," J. Appl. Phys. **97**, 013538 (2005).
45. J. Bogdanowicz, M. Gilbert, N. Innocenti, S. Koelling, B. Vanderheyden, and W. Vandervorst, "Light absorption in conical silicon particles," Opt. Express **21**, 3891–3896 (2013).
46. M. Huang, Y. Cheng, F. Zhao, and Z. Xu, "The significant role of plasmonic effects in femtosecond laser-induced grating fabrication on the nanoscale," Ann. Phys. **S25**, 74–86 (2013).
47. A. Vorobyev and C. Guo, "Antireflection effect of femtosecond laser-induced periodic surface structures on silicon," Opt. Express **19**, A1031–A1036 (2011).
48. J. Bonse, "All-optical characterization of single femtosecond laser-pulse-induced amorphization in silicon," Appl. Phys. A **84**, 63–66 (2006).
49. A. Esser, W. Kütt, M. Strahnen, G. Maidorn, and H. Kurz, "Femtosecond transient reflectivity measurements as a probe for process-induced defects in silicon," Appl. Surf. Sci. **46**, 446–450 (1990).
50. S. Sundaram and E. Mazur, "Inducing and probing non-thermal transitions in semiconductors using femtosecond laser pulses," Nat. Mater. **1**, 217–224 (2002).
51. D. von der Linde and K. Sokolowski-Tinten, "The physical mechanisms of short-pulse laser ablation," Appl. Surf. Sci. **154–155**, 1–10 (2000).

1. Introduction

The irradiation of solids with multiple linear polarized femtosecond laser pulses at fluences close to the damage threshold leads to the formation of laser-induced periodic surface structures (LIPSS) on the surface of almost all materials [1–5]. Two distinct types of LIPSS are observed upon femtosecond laser pulse irradiation. For strong absorbing materials such as metals or semiconductors, in most cases low-spatial-frequency LIPSS (LSFL) are observed with a period Λ_{LSFL} close to the irradiation wavelength λ [1,3,5]. These LSFL are generated by interference of the incident laser beam with a surface electromagnetic wave (SEW) generated at a rough surface [6,7]. In contrast, on dielectrics, often high-spatial-frequency LIPSS (HSFL) with spatial periods significantly smaller than the irradiation wavelength ($\Lambda_{HSFL} < \lambda/2$) have been observed [2,8]. The origin of the HSFL is controversially discussed in the literature [1,8,9].

On silicon, predominantly LSFL were observed after low repetition rate ($\leq$ 1 kHz) Ti:Sapphire femtosecond laser pulse irradiations in air environment [2, 10–14]. Their orientation is perpendicular to the laser beam polarization and the periods typically range between $\sim 0.6\lambda$ and λ, depending on the degree of material excitation [13,15], and the number of laser pulses per spot [14]. Several authors have suggested that these structures are caused by excitation of surface plasmon polaritons (SPP) at the air - silicon interface when the material turns from a semiconducting into a metallic state [3, 13, 16]. The interference between the electromagnetic field of the SPP and the incident laser pulse leads to a spatially modulated deposition of optical energy to the electronic system of the material. After coupling to the lattice system [17] and subsequent ablation processes, this results in a periodically corrugated surface topography [18]. The corresponding LSFL modulation depths are typically of the order of the

#197904 - $15.00 USD Received 17 Sep 2013; revised 23 Oct 2013; accepted 27 Oct 2013; published 22 Nov 2013

optical penetration depth in the laser-excited material ($\sim$ 100 nm) [19, 20], which is consistent with the plasmonic scenario acting at the air-silicon interface.

Two different experimental approaches were reported to study the dynamics of the LSFL formation upon irradiation of silicon by ultrashort laser pulses. Recently, in a femtosecond XUV scattering (pump-probe) experiment after single pulse irradiation of a thin silicon film, evidence for intrapulse energy deposition at specific spatial frequencies (associated with LSFL) was presented [21]. In a second approach [22, 23], multiple equal energy double-fs-pulse sequences of variable delay were used to elucidate the importance of *inter*- and *intra*-pulse feedback phenomena [24]. For silicon, the LSFL spatial period does not significantly depend on the double-pulse delay Δt [23], while the LSFL rippled area strongly decreased with increasing delays up to several picoseconds [22]. In the latter work, two characteristic exponential decay times of ~ 0.15 ps and ~ 11 ps were found.

In this work, we extend a recently developed model [15, 25] into a double-pulse excitation scheme in order to calculate the carrier dynamics and to investigate the involvement of SPP excitation in LSFL formation on crystalline silicon. The method allows to quantify the SPP active area for different delays which is compared with experimental results. The importance of carrier generation and relaxation processes in the conduction band is demonstrated.

2. Theoretical model

Upon high-intensity laser irradiation of crystalline silicon with femtosecond laser pulses, electrons can be promoted from the valence band (VB) to the conduction band (CB) via linear and nonlinear optical absorption effects. Once a sufficiently large amount of electrons is promoted, the optical properties (e.g. the complex dielectric permittivity ε_{Si}^{*}) are affected. In presence of such a dense electron-hole plasma at CB electron densities $N_e \gtrsim 4 \times 10^{21}$ cm^{-3}, the silicon transiently turns from a semiconducting to a metal-like high-reflective state [13, 26, 27].

Surface plasmon polaritons can be excited at the air / excited silicon interface when the real part of the dielectric permittivity falls below minus one [28], as expressed by :

$$\Re e\left[\varepsilon_{Si}^{*}\right] < -1 \tag{1}$$

This occurs when a threshold carrier density N_{th}^{SPP} is exceeded. As usually Gaussian beam profiles are used, the spatial distribution of laser-induced electrons in the CB along with the threshold defines an "SPP active area" ($\mathscr{A}_{SPP}$) in which surface plasmon polaritons can be excited. This idea is illustrated in Fig. 1, where the hatched circular zone represents $\mathscr{A}_{SPP}$. Using numerical methods, the temporal evolution of the $\mathscr{A}_{SPP}$ can be evaluated for different double-pulse delays.

2.1. Description of optical properties

The dielectric permittivity of laser-excited silicon ε_{Si}^{*} with carrier densities N_e up to 10^{22} cm^{-3} can be described using a Drude model given by [27]

$$\varepsilon_{Si}^{*}(N_e) = \varepsilon_{Si} - \frac{\omega_p^2(N_e)}{\omega^2\left(1 + i\frac{\nu}{\omega}\right)}, \tag{2}$$

where $\varepsilon_{Si} = 13.64 + 0.048i$ is the dielectric constant of the non-excited silicon at $\lambda = 800$ nm wavelength [29], ω_p is the plasma frequency defined as $\omega_p = \sqrt{N_e e^2/(m_e^{*}\varepsilon_0)}$ [e: electron charge, $m_e^{*} = 0.18 \times m_e$: effective optical mass, m_e: free electron mass, ε_0: dielectric permittivity of the vacuum], $\nu^{-1} = 1.1$ fs is the carrier collision time in laser-excited silicon [27], and ω is the laser angular frequency. Band filling and band gap renormalization effects are neglected here.

#197904 - $15.00 USD Received 17 Sep 2013; revised 23 Oct 2013; accepted 27 Oct 2013; published 22 Nov 2013

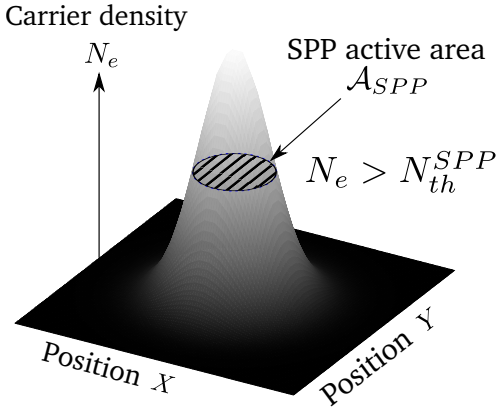

Fig. 1. Scheme of typical free-carrier density distribution at the surface of silicon during laser pulse irradiation. The hatched circular zone corresponds to the area on which surface plasmon polaritons (SPP) can be excited while the free-carrier density N_e is greater than the threshold density for SPP excitation N_{th}^{SPP} at the interface between air and silicon.

In order to consider intrapulse changes of the surface reflectivity of silicon, a multilayer model was used for normal incident radiation. The laser-excited region is considered as a layered structure where each layer j has its own optical properties (related to the local free-carrier density), as defined in Eq. (2). The fraction of the laser wave amplitude reflected at the interface between layers j and k is calculated by the recurrence formula [30, 31]

$$r_{j,k} = \frac{r_{j,j+1} + r_{j+1,k} e^{2i\phi_{j+1}}}{1 + r_{j,j+1} r_{j+1,k} e^{2i\phi_{j+1}}}, \tag{3}$$

where $r_{j,j+1}$ is given by Fresnel equations [32]. $\phi_{j+1} = \frac{2\pi h_{j+1}}{\lambda} \times \sqrt{\varepsilon_{j+1}}$ is the phase shift induced by the $j+1$ layer of thickness h_{j+1}. The final value of the surface reflectivity R is determined by $R = |r_{0,N}|^2$ where 0 corresponds to air and N is a layer located at a depth significantly larger than the optical penetration depth.

2.2. *Free-carrier dynamics*

The electron density in the conduction band N_e was calculated considering one- and two-photon absorption, carrier diffusion and Auger recombination by solving the following partial differential equation [15]

$$\frac{\partial N_e}{\partial t} = \nabla \left(k_B T_e \mu_e \nabla N_e \right) + G_e - R_e. \tag{4}$$

$G_e = \frac{\sigma_1 I}{\hbar\omega} + \frac{\sigma_2 I^2}{2\hbar\omega}$ describes the electron generation rate using the one-photon (σ_1) and two-photon (σ_2) absorption coefficients listed in Table 1. $I \equiv I(t,z)$ is the temporal intensity profile within the sample upon laser excitation. $R_e = \frac{N_e}{\tau_{AR} + \left(C_{AR} N_e^2\right)^{-1}}$ describes the loss rate of CB electrons by Auger recombination [25], where $\tau_{\mathrm{AR}} = 6$ ps is the minimal recombination time due to plasma screening [33, 34] and $C_{AR} = 3.8 \times 10^{-43}$ m^6/s is the Auger recombination coefficient [35]. The first term on the right-hand side of Eq. (4) describes the carrier transport due to diffusion where $\mu_e = e/(m_e^* \nu)$ is the carrier mobility in the CB, and k_B is the Boltzmann constant. Avalanche ionization has been neglected here.

#197904 - $15.00 USD Received 17 Sep 2013; revised 23 Oct 2013; accepted 27 Oct 2013; published 22 Nov 2013

Table 1. Material parameters used in numerical simulations of femtosecond laser-irradiated silicon (wavelength $\lambda = 800$ nm, pulse duration $\tau = 150$ fs).

Coefficient	Symbol	Value	Unit	Reference
Band gap energy	E_g	1.12	eV	[30]
Dielectric constant of crystalline silicon	ε_{Si}	$13.64 + 0.048i$	–	[29]
One-photon absorption coefficient	σ_1	1.021×10^5	m^{-1}	[29]
Two-photon absorption coefficient	σ_2	6.8×10^{-11}	m/W	[36]
Carrier collision time	ν^{-1}	1.1×10^{-15}	s	[27]
Effective optical mass	m_e^*	1.64×10^{-31}	kg	[27]
Auger recombination rate	C_{AR}	3.8×10^{-43}	m^6/s	[35]
Minimum Auger recombination time	τ_{AR}	6.0×10^{-12}	s	[34]
Minimum electron-phonon coupling time	τ_γ^0	240×10^{-15}	s	[33]
Threshold density for electron-phonon coupling	N_{th}	6.02×10^{26}	m^{-3}	[33]

The intensity in the sample is calculated by numerically solving the equation

$$\frac{dI}{dz} = -(\sigma_1 I + \sigma_2 I^2). \tag{5}$$

The intensity at the sample surface is $I(t, z = 0) = [1 - R]\, I_0(t)$, where R is the surface reflectivity at $\lambda = 800$ nm described in the previous Section 2.1 and the incident laser intensity I_0 is given by the temporal double-fs-pulse profile via

$$I_0(t) = \frac{F_0}{\tau}\sqrt{\frac{4\ln 2}{\pi}}\left[e^{-\frac{1}{2}\left(\frac{t-t_1}{\sigma_\tau}\right)^2} + e^{-\frac{1}{2}\left(\frac{t-t_2}{\sigma_\tau}\right)^2}\right]. \tag{6}$$

In this superposition of two individual temporally Gaussian pulses of duration τ (full width at half maximum, FWHM), F_0 denotes the peak fluence of each individual pulse of the double-pulse sequence. $t_{1,2}$ denotes the time when the two individual pulse maxima are reached. Then $\Delta t = t_2 - t_1$ defines the double-pulse delay. Note that the first pulse is centered at $t_1 = 0$ fs. Here, σ_τ is given by $\tau/(2\sqrt{2\ln 2})$. For the numerical calculations, a pulse duration $\tau = 150$ fs was selected to match the experimental conditions given in Ref. [22].

2.3. Energy relaxation

The free-carrier dynamics is additionally affected by carrier diffusion and energy relaxation, which both strongly depend on the temperature. To calculate temperatures of the free-carriers T_e and the silicon lattice T_{Si}, a two-temperature model was used. It is assumed here that CB electrons and VB holes both have the same temperature, i.e., T_e. A partial differential equation was used to describe the temperature distribution of the free-carriers given by [25, 30]

$$C_e \frac{\partial T_e}{\partial t} = \nabla(\kappa_e \nabla T_e) - \gamma(T_e - T_{Si}) + Q_e, \tag{7}$$

where $\kappa_e = 2k_B \mu_e N_e T_e / e$ is the free-carrier thermal conductivity. The specific heat capacity of the free-carriers is given by $C_e = \frac{3}{2} k_B N_e$. The energy coupling rate between free-carriers and lattice is $\gamma = \frac{C_e}{\tau_\gamma}$, with $\tau_\gamma = \tau_\gamma^0\left[1 + \left(\frac{N_e}{N_{th}}\right)^2\right]$, $N_{th} = 6.02 \times 10^{20}$ cm^{-3} and $\tau_\gamma^0 = 240$ fs [25, 33]. According to recent experiments, τ_γ has been limited to 2 ps at high carrier densities [37].

#197904 - $15.00 USD Received 17 Sep 2013; revised 23 Oct 2013; accepted 27 Oct 2013; published 22 Nov 2013

The laser source term $Q_e = \left[(\hbar\omega - E_g)\frac{\sigma_1 I}{\hbar\omega} + (2\hbar\omega - E_g)\frac{\sigma_2 I^2}{2\hbar\omega}\right] + E_g R_e - \frac{3}{2}k_B T_e \frac{\partial N_e}{\partial t}$ taken from [25] considers the one- and two-photon absorption of the laser beam, the release of energy ($E_g R_e$) due to Auger recombination (band gap energy $E_g = 1.12$ eV), and the last term accounts for the N_e-dependent change of the electronic heat capacity. Free-carrier heating has been neglected.

The lattice temperature T_{Si} is calculated by solving the partial differential equation [30]:

$$C_{Si}\frac{\partial T_{Si}}{\partial t} = \nabla(\kappa_{Si}\nabla T_{Si}) + \gamma(T_e - T_{Si}). \tag{8}$$

The second term on the right hand side of Eqs. (7) and (8) considers energy transfer between the free-carriers and the lattice via electron-phonon coupling. The heat capacity of silicon C_{Si} and thermal conductivity κ_{Si} both depend on the liquid density fraction η in the laser-excited volume and were calculated here via $C_{Si}(T_{Si}) = (1-\eta)C_{Si}^{(s)}(T_{Si}) + \eta C_{Si}^{(l)}(T_{Si})$ and $\kappa_{Si}(T_{Si}) = (1-\eta)\kappa_{Si}^{(s)}(T_{Si}) + \eta\kappa_{Si}^{(l)}(T_{Si})$. For non-molten (solid) silicon, the heat capacity $C_{Si}^{(s)}$ and the thermal conductivity $\kappa_{Si}^{(s)}$ are given by $C_{Si}^{(s)}$[J/(m^3·K)]$= 1.978\times10^6 + 3.54\times10^2 T_{Si} - 3.68\times10^6 T_{Si}^{-2}$ and $\kappa_{Si}^{(s)}$[W/(m·K)]$= 1.585\times10^5 T_{Si}^{-1.23}$, respectively [35]. For the liquid state, the corresponding parameters are $C_{Si}^{(l)}(T_{Si}) = 2.633\times10^6$ J/(m^3·K) [38] and $\kappa_{Si}^{(l)}(T_{Si})$[W/(m·K)]$= 50.2 + 29.3\times10^{-3}(T_{Si} - T_m)$ [39]. The melting temperature T_m of silicon is 1687 K at ambient pressure [40]. Melting is considered in the model of laser heating here by keeping the local temperature constant at T_m until the internal energy increase reaches the melting enthalpy $\Delta H_m = 4.2\times10^9$ J/m^3 [41].

The boundary conditions for free-carrier transport and thermal energy diffusion were implemented so that free-carriers and energy do not leave the sample of 400 μm thickness. The initial temperature of the system was set to 300 K. The numerical code for solving the partial differential Eqs. (4), (7), and (8) was developed by using the method of finite volumes [42]. The calculations were performed in a one-dimensional approach in the direction normal to the sample surface. The time integration was performed using an implicit scheme. Equation (5) has been solved using a Runge-Kutta 4th-order algorithm [43]. The numerical time-step δt has been decreased until convergence of the solutions was reached ($\delta t = 10^{-16}$ s). A non-uniform mesh size was used with smaller cells close to the surface. For simplified cases, the validity of the numerical code has been verified with analytical solutions and energy balance monitoring.

2.4. Quantification of the SPP active area

The numerical calculations were performed for different laser fluences F_0 up to 0.7 J/cm^2. For each fluence, the delay Δt between the two $\tau = 150$ fs pulses was systematically varied between 0 and 3.5 ps.

For quantification of the SPP active area, the following four steps were conducted.

1. For each laser fluence F_0, and double-pulse-delay Δt, the free-carrier density N_e was calculated as a function of time (up to $t = 5$ ps). Since the proposed mechanism of LSFL formation involves the excitation of SPP and their interference with the incident laser beam [13], the carrier density $N_e^{t_{max}}(F_0, \Delta t)$ was identified just at the end of the second femtosecond laser pulse, i.e., at the time t_{max} when its intensity dropped to a fraction ζ of its maximum value $[I_0(t_{max}) = \zeta \times \max\{I_0(t)\} = \zeta \times F_0/\tau \times \sqrt{4\ln 2/\pi}]$. As the interference between the laser and the SPP electromagnetic field should be remarkable, the value of ζ is expected to be close to unity.

2. As a Gaussian beam with radius w_0 having a spatial fluence profile of $F(r) = F_0 e^{-2\left(\frac{r}{w_0}\right)^2}$

#197904 - $15.00 USD Received 17 Sep 2013; revised 23 Oct 2013; accepted 27 Oct 2013; published 22 Nov 2013

was used, the relation between radial coordinate r and the local fluence F is given by

$$r(F) = w_0 \sqrt{\frac{1}{2} \ln\left(\frac{F_0}{F}\right)} \tag{9}$$

3. In the next step, for each fluence F, the radial coordinate $r(F)$ was calculated according to Eq. (9), and associated with the corresponding value $N_e^{t_{max}}(F, \Delta t)$. In this way, a curve $N_e^{t_{max}}(r(F), \Delta t)$ was constructed.

4. Then, the implicit equation

$$N_e^{t_{max}}(r(F), \Delta t) = N_{th}^{SPP} \tag{10}$$

was solved, where N_{th}^{SPP} is the threshold carrier-density necessary for SPP excitation. The value of N_{th}^{SPP} is directly calculated from Eq. (2) using the criterion $\Re e\left[\varepsilon_{Si}^*\left(N_{th}^{SPP}\right)\right] = -1$, which can be written as [16]

$$N_{th}^{SPP} = \frac{m_e^* \varepsilon_0 \left(\Re e\left[\varepsilon_{Si}\right] + 1\right)}{e^2} \left(\omega^2 + \nu^2\right) \tag{11}$$

Using the parameters introduced in Section 2.1, $N_{th}^{SPP} = 5.27 \times 10^{21}$ cm^{-3} is found. With that value, the solution of Eq. (10) provides the SPP excited radius $r_{SPP}(\Delta t)$ as a function of the double-pulse delay Δt. Finally, assuming a circular shape of the SPP active area, $\mathscr{A}_{SPP}$ is calculated via

$$\mathscr{A}_{SPP}(\Delta t) = \pi r_{SPP}^2(\Delta t). \tag{12}$$

3. Results and discussion

In this section, the results of the numerical calculations based on the model given in the previous Section 2 are presented. The free-carrier density N_e is calculated as a function of time t, laser fluence F_0, and double-pulse delay Δt. First, the effect of a double-pulse irradiation on the free-carrier density at the surface is analyzed, before the SPP active area is quantitatively evaluated as function of the double-pulse delay and compared to experimental data of the LSFL rippled area.

Figure 2 exemplifies the results of the numerical calculations of the free-carrier density N_e at the silicon surface upon irradiation with double-pulses of Δt = 0.5 ps delay and with three different fluences $F_0 = 0.2$, 0.3, and 0.5 J/cm^2. The upper graph visualizes the temporal evolution of N_e (left ordinate) on short timescales up to 1 ps, while the lower graph displays the carrier dynamics at longer timescales up to 5 ps. In both graphs the temporal intensity profile of the double-fs-pulse sequence is added for comparison (right ordinate). As seen in Fig. 2(a), the maximum carrier density is reached during the second laser pulse and increases with F_0. For the lowest fluence of $F_0 = 0.2$ J/cm^2, the threshold density N_{th}^{SPP} is not reached, while for $F_0 = 0.3$ J/cm^2 it is exceeded during the second pulse. For $F_0 = 0.5$ J/cm^2, it is passed already during the first laser pulse. Moreover, the decrease rate $(\partial N_e/\partial t)$ of the carrier density between the two individual femtosecond laser pulses is faster at higher fluences F_0. This is attributed to Auger recombination and thermal carrier diffusion which are more efficient at larger carrier densities (recombination) and larger electron temperatures (diffusion). The two mechanisms also account for the carrier density decrease after the second laser pulse, as seen at large times in Fig. 2(b). For all selected fluences and at the given delay, the second pulse increases the carrier density N_e above the level generated by the first one.

Similar calculations have been performed by systematically varying the laser fluence F_0 (0.15 J/cm^2 - 0.70 J/cm^2) and the double-pulse delay Δt (0 ps - 3.5 ps). Figure 3 visualizes all the results by plotting the maximum of the free-carrier density N_e^{max} as a function of both parameters

#197904 - $15.00 USD Received 17 Sep 2013; revised 23 Oct 2013; accepted 27 Oct 2013; published 22 Nov 2013

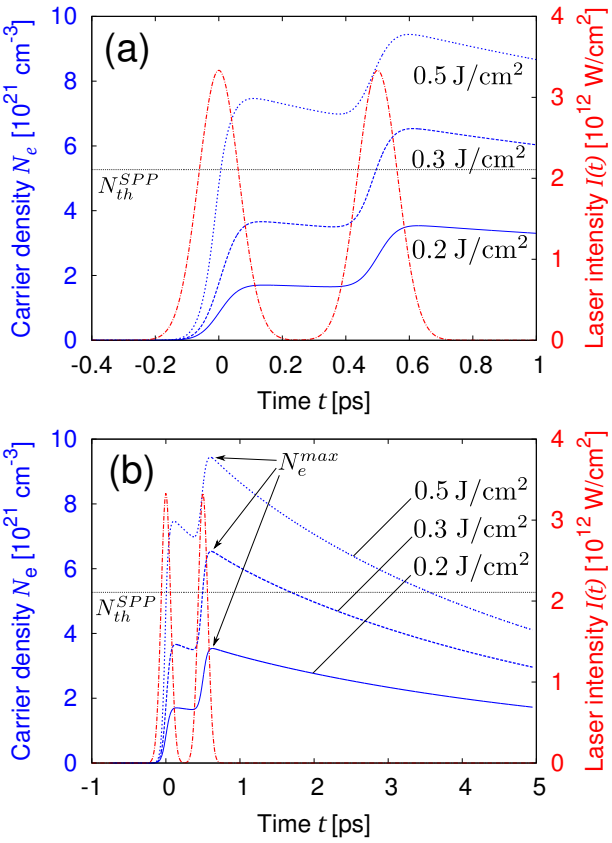

Fig. 2. Evolution of the free-carrier density (left ordinates) at the surface of silicon irradiated by a femtosecond double-pulse with a delay of $\Delta t = 0.5$ ps and single pulse fluence of $F_0 = 0.2$, 0.3 and 0.5 J/cm^2 (pulse duration $\tau = 150$ fs, laser wavelength $\lambda = 800$ nm). (a) Short timescales up to 1 ps. (b) Long timescales up to 5 ps. For comparison, the temporal double-pulse intensity profile is shown (right ordinates). The horizontal lines indicate the threshold density N_{th}^{SPP} for SPP excitation. The maximum values of the carrier density N_e^{max} are marked in (b).

in a false-colour map. The solid black isoline indicates where the carrier density equals the SPP threshold density N_{th}^{SPP}. Above $F_0 = 0.17$ J/cm^2, this threshold can be exceeded.

Figure 4 represents a vertical cross section at $F_0 = 0.25$ J/cm^2 through the data previously shown in Fig. 3. Two regimes can be distinguished in the evolution of the maximum carrier density with the delay, i.e., a fast decrease within less than 0.15 ps and a slow decrease with a time constant of approximately 8 ps (see the red solid curve). A variation of the model parameters reveals that the fast decay is caused by the nonlinear (two-photon) absorption in the silicon. As the two-photon absorption scales quadratically with the laser beam intensity (see Eq. (5)), it increases the number of laser-generated carriers especially for small delays when the two 150-fs laser pulses are temporally overlapping. Moreover, individually disabling the physical processes confirms that the slow area decrease originates from both the thermal diffusion of carriers and from Auger recombination. The two additional (dashed green and dotted blue) curves represent the values of $N_e^{t_{max}}$ calculated according to step 1 in Section 2.4 for two very different intensity-decay levels $\zeta = 50\%$ and 99%. While the curve of $N_e^{t_{max}}$ for $\zeta = 50\%$ almost coincides with N_e^{max}, the curve for $\zeta = 99\%$ decays faster with Δt. This demonstrates

#197904 - $15.00 USD Received 17 Sep 2013; revised 23 Oct 2013; accepted 27 Oct 2013; published 22 Nov 2013

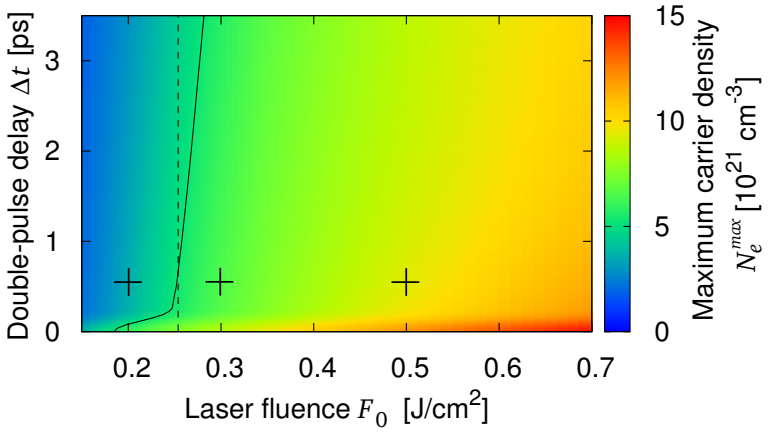

Fig. 3. Maximum free-carrier density as a function of laser fluence F_0 and double-pulse delay Δt. The black isoline represents the SPP threshold density N_{th}^{SPP}. The three crosses indicate the parameters used in Fig. 2. (Irradiation parameters: $\tau = 150$ fs, $\lambda = 800$ nm). The vertical dashed line corresponds to the data displayed in Fig. 4.

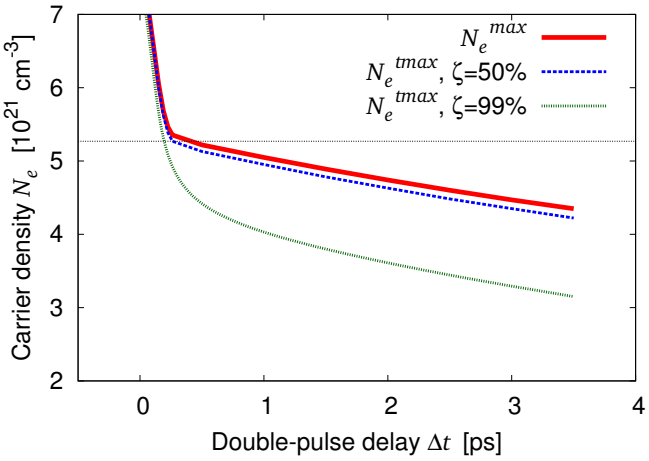

Fig. 4. Maximum free-carrier density N_e^{max} as a function of the double-pulse delay Δt (red solid line). The dashed blue and dotted green represent $N_e^{t_{max}}$ calculated for $\zeta = 50\%$ and 99%, respectively. Model parameters: $F_0 = 0.25$ J/cm^2, $\tau = 150$ fs, $\lambda = 800$ nm. The dotted horizontal line indicates the threshold density N_{th}^{SPP} for SPP excitation.

that ζ in the temporal interference criterion (see step 1 in Section 2.4) is important here and should be systematically varied in the comparison of the SPP active area $\mathscr{A}_{SPP}$ and the LSFL rippled area $\mathscr{A}_{LSFL}$.

Following the complete procedure (steps 1 – 4) described in Section 2.4, the SPP active area has been calculated for the different values of $\zeta = 50\%$, 90% and 99%. Figure 5(a) visualizes the calculated results of $\mathscr{A}_{SPP}$ as a function of the double-pulse delay Δt (red curves) along with the experimental data reported in Ref. [22] for the LSFL rippled area after irradiation of silicon by a sequence of 15 double-pulses, each at a total peak fluence of $F_{0,tot} = 2 \times F_0 = 0.3$ J/cm^2 (blue data points). Figure 5(b) shows three representative scanning electron micrographs of the LSFL rippled areas obtained under these conditions for $\Delta t = 0$ ps, 0.7 ps, and 2 ps. A

#197904 - $15.00 USD Received 17 Sep 2013; revised 23 Oct 2013; accepted 27 Oct 2013; published 22 Nov 2013

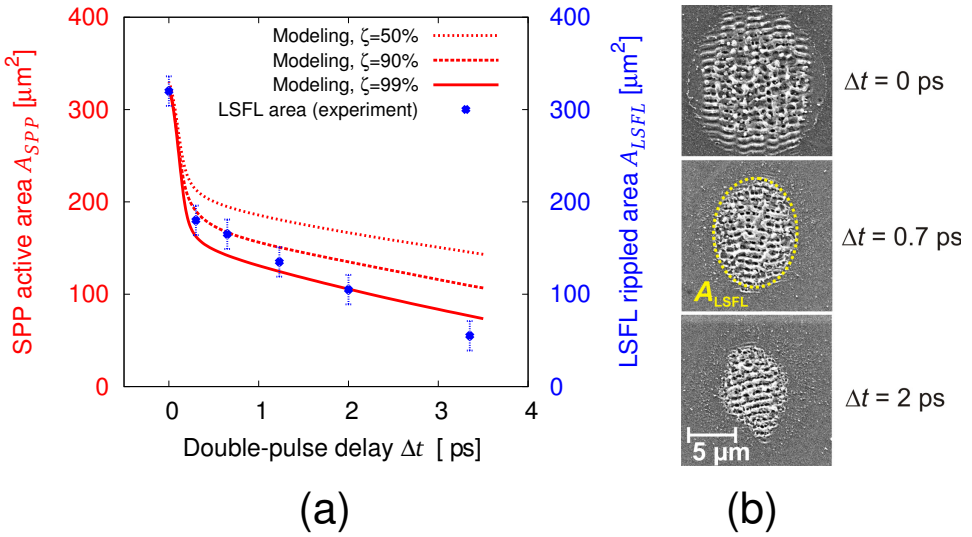

Fig. 5. Calculated SPP active area $\mathscr{A}_{SPP}$ as a function of the double-pulse delay Δt for three different values of $\zeta = 50\%$, 90% and 99%) (a). The blue data points of the LSFL rippled area $\mathscr{A}_{SPP}$ are taken from [22] for comparison. Model parameters: $F_0 = 0.40$ J/cm^2, $\tau = 150$ fs, $\lambda = 800$ nm, $w_0 = 16.5$ μm. In (b), representative scanning electron micrographs for delays up to 2 ps are shown. The LSFL rippled area is marked at $\Delta t = 0.7$ ps.

quantitative agreement between $\mathscr{A}_{SPP}$ and $\mathscr{A}_{LSFL}$ is obtained for $\zeta = 99\%$. It must be noted here that the optimum agreement with the experimental data was obtained for $F_0 = 0.40$ J/cm^2 which is more than two times larger than the single-pulse fluence $F_0 = 0.15$ J/cm^2 used experimentally.

In order to explain this discrepancy between the experimental and theoretical fluence values, some additional aspects must be considered. The numerical calculations performed here assume the interaction *of a single* double-fs-pulse with a geometrically flat surface of single-crystalline silicon. However, in the experiments, multiple double-pulse sequences were required to form the LSFL at the surface resulting in a periodically corrugated surface. Typically, a few incubating pulses are needed to reach the ablation condition and to generate a rough surface [44]. Additional laser pulses then form the LSFL via scattering and SPP excitation and further reinforce the grating-like surface morphology via inter-pulse feedback [14, 24].

Upon irradiation with multiple laser pulses, the maximum number of laser-induced carriers generated at the surface will be additionally affected by several inter- and intra-pulse effects – even if the laser peak fluence ($F_{0,tot}$) is kept constant during the pulse irradiation sequence:

1. *Incubation effects (inter-double-pulse)*: Due to incubation effects, the damage threshold fluence of the material F_{th} decreases with increasing number of (single) laser pulses [30]. For Ti:sapphire 130-fs laser pulse irradiation of silicon, this effect was studied already in detail in [10]. For less than $N = 1000$ laser pulses, an incubation law of the form $F_{th}(N) = F_{th}(1) \times N^{\xi-1}$ was found, with the single-pulse damage threshold $F_{th}(1) = 0.26$ J/cm^2 and an incubation coefficient $\xi = 0.84$ [10]. As a result, for a fixed fluence F_0, the ratio F_0/F_{th} increases, resulting in a larger number of laser-generated carriers at the silicon surface. Hence, for $N = 15$ laser pulses as used in [22], the threshold ratio $F_{th}(1)/F_{th}(15)$ is ~ 1.5. Considering this effect along with the somewhat different pulse duration ($\tau = 150$ fs), the numerical calculations indicate that the experimental value of $F_0 = 0.15$ J/cm^2 used in [22] for the multiple pulse irradiation is equivalent to the

#197904 - $15.00 USD Received 17 Sep 2013; revised 23 Oct 2013; accepted 27 Oct 2013; published 22 Nov 2013

irradiation by an increased *effective* single-pulse fluence of 0.27 J/cm^2.

2. *Geometrical surface modifications (inter-double-pulse):* Once the initially flat silicon surface becomes corrugated due to ablation after a certain number of double-pulse sequences, the next laser pulse will significantly change its interaction (absorption) due to geometrical effects. As in the vicinity of sharp features of the surface topography a significant enhancement of the electromagnetic field (by factors up to 10) can occur [19, 45, 46], the spatial carrier density distribution may become inhomogeneous and increases locally at a rough or rippled surface. Along with the increased optical absorption, also the sample reflectivity decreases due to the geometrical corrugation from initially $R_{flat} = 0.33$ for a flat silicon surface at normal incidence ($\lambda = 800$ nm) down to values below $R_{corr} < 0.1$ [47]. However, even for a perfectly absorbing surface ($R_{corr} = 0$) the latter effect can increase the absorbed laser pulse energy by up to 50 % [(1-R_{corr})/(1-R_{flat})=(1-0)/(1-0.33)=1.5].

3. *Structural surface modifications (inter-double-pulse):* Upon laser pulse irradiation in the ablative regime, also a residual melt layer is left at the surface which resolidifies after each double-pulse impact. For (single-pulse) fluences below 0.58 J/cm^2, a superficial amorphous layer of some tens of nanometer thickness is formed at the surface which exhibits a surface reflectivity increased by up to a few percent and which has a 25-times increased linear absorption coefficient compared to crystalline silicon [48]. This inter-pulse effect additionally may increase the number of laser-induced carriers, as due to the amorphization, the optical absorption occurs in a reduced energy deposition depth. Moreover, laser-generated structural effects in the silicon lattice can lead to trapping of carriers by defect states on the picosecond timescale [49].

4. *Phase transitions (intra-double-pulse):* If the delay between the first and the second pulse of the double-pulse sequence is large enough, thermal phase transitions will occur if the fluence of the first pulse is sufficiently high. Thermal melting of semiconductors was shown to occur on the timescale of a few picoseconds [50] while ablation starts typically after tens to hundreds of picoseconds [51]. This effect can contribute to deviations between the experimentally observed LSFL area and the calculated SPP active area. Above a certain number of double-pulse sequences, the silicon melts already after the first pulse. The optical surface properties then turn within a few picoseconds to that of metal with a few nanometer optical penetration depth only acting during the second laser pulse. As the energy deposition depth is simultaneously decreased, the energy of the second pulse is deposited in a layer excited by the first pulse already, which later undergoes almost complete ablation and is, therefore, not contributing to the LSFL topography. In this way, the effect may shield the pulse energy of the second pulse when melting occurs between the two fs-laser pulses.

The theoretical description of these intra- and inter-pulse effects in multiple irradiation sequences is beyond the scope of this work. However, the discussed effects justify that the fluence F_0 was varied systematically in the numerical calculations to obtain the best match between the SPP active area and the LSFL rippled area.

4. Conclusions

The laser-induced carrier dynamics in the conduction band of silicon upon irradiation with femtosecond double-pulse sequences of varying delays up to ~ 4 ps was numerically calculated using the two-temperature model, considering carrier generation via one- and two-photon absorption, carrier diffusion and Auger recombination effects as well as their impact on the

#197904 - $15.00 USD Received 17 Sep 2013; revised 23 Oct 2013; accepted 27 Oct 2013; published 22 Nov 2013

transient optical properties. At sufficiently high laser fluences, the semiconducting material transiently turns to a metallic state allowing the excitation of surface plasmon polaritons. Additionally taking into consideration a spatially Gaussian beam profile along with an interference criterion between the laser and the plasmon electromagnetic fields, the SPP active area was quantified as a function of the double-pulse delay and compared to experimental data of the LSFL rippled area observed in recent experiments. Both the SPP active area and the LSFL area show two characteristic decay-times – one of $\tau_1 \sim 0.147$ ps and another one of $\tau_2 \sim 13.0$ ps. Quantitative agreement between both the experiments and calculations was obtained when multi-pulse driven inter- and intra-pulse feedback effects are considered. Our results directly support the SPP-based LSFL formation mechanism proposed earlier for silicon and identify the nonlinear (two-photon) absorption to be responsible for the rapid area decrease (τ_1) while carrier diffusion and Auger recombination effects account for the slower area decrease (τ_2). The temporally resolved calculations of the carrier dynamics manifest that the intra-pulse energy deposition step is responsible for the spatial characteristics of the rippled surface which is later reinforced through inter-pulse feedback.

Acknowledgments

T.J.-Y.D. acknowledges a postdoctoral fellowship awarded by the Adolf-Martens-Fond e.V. The authors would like to thank M. Tischer (MBI) for taking the SEM images. This work was supported by the German Science Foundation (DFG) under Grant Nos. RO 2074/7-2 and KR 3638/1-2.

#197904 - $15.00 USD Received 17 Sep 2013; revised 23 Oct 2013; accepted 27 Oct 2013; published 22 Nov 2013